Soft Matter

Accepted Manuscript

This is an *Accepted Manuscript*, which has been through the Royal Society of Chemistry peer review process and has been accepted for publication.

Accepted Manuscripts are published online shortly after acceptance, before technical editing, formatting and proof reading. Using this free service, authors can make their results available to the community, in citable form, before we publish the edited article. We will replace this *Accepted Manuscript* with the edited and formatted *Advance Article* as soon as it is available.

You can find more information about *Accepted Manuscripts* in the **Information for Authors**.

ROYAL SOCIETY OF CHEMISTRY

www.rsc.org/softmatter

Flow of concentrated viscoelastic polymer solutions in porous media: effect of MW and concentration on elastic turbulence onset in various geometries.

Andrew M Howe, Andrew Clarke, Daniel Giernalczyk

Schlumberger Gould Research

Abstract

Viscoelastic polymer solutions exhibit a variety of flow instabilities and in particular, in mixed shear and extensional flow, elastic turbulence. Coincident with the transition to turbulence is additional dissipation that, in porous flow, may be characterised as an increased apparent viscosity. We report elastic turbulence and apparent thickening in the flow of polymer solutions both in rock samples and in microfluidic analogues and we correlate the onset of thickening and turbulence with rheological measurements. Contrary to expectations, the characteristic relaxation time associated with the transition to turbulence is found to be independent of polymer concentration over the range studied $(10c^* \lesssim c \lesssim 100c^*)$. Furthermore, this characteristic time scales with the square of molecular weight. Thus the characteristic time associated with the transition to turbulence is not the linear-viscoelastic timescale usually measured but rather scales as a dilute Rouse time despite being an entangled system.

1   Introduction

Aqueous polymer solutions are of wide interest because of their broad industrial applications and their rich physicochemical behaviours. Fluid flows in porous media display a variety of physical phenomena and are key to many natural and commercial processes spanning multiple fields including physics, geophysics, medicine, and chemical engineering [1] [2] [3] [4] [5] [6] [7]. Here we address the phenomenology of flow of high molecular weight polymer solutions through porous structures at concentrations well above c^*, the overlap concentration. The motivation for this study is the desire to understand the role of viscoelastic polymer solutions in enhanced oil recovery (EOR) [7]. Oil recovery is usually characterised as proceeding through three steps of systematically increasing technological complexity. First, when a well is drilled into an oil-bearing porous rock (the reservoir), natural pressure in the system is sufficient to raise the oil to the surface and a few percent of the oil in the reservoir may be recovered. Second, water is pumped (injected) into the reservoir either to maintain the reservoir pressure such that oil continues to come to the surface (be "produced") or to sweep oil in the porous structure toward the producing well. This "water-flooding" process can recover up to a further ~30% of the oil originally in the reservoir. Third, to produce more of the 60-70% of the oil remaining in the reservoir, an enhanced oil recovery process must be employed. EOR technologies fall into three general categories: chemical, thermal and gas. For chemical technologies, polymer injection is the simplest from an engineering point of view. Polymers are generally used with the concept of simply "viscosifying" the aqueous phase whilst not considering their viscoelastic properties. A range of polymer types have been employed, usually at concentrations ranging well above $10c^*$, i.e. well into the entangled region for a neutral polymer. This technology has been used for many years, particularly in China. Recently it has been reported [8], [9], [10] that high-viscosity, viscoelastic solutions of high molecular weight (MW = 20 - 35 MDa) polymers recover significantly more oil than expected from conventional models of the process. Our recent findings [11] have provided confirmation of this behaviour and demonstrated that a key additional behaviour not captured in both conventional and proposed models is the appearance of elastic turbulence.

Solutions of high molecular weight flexible polymers are well known to exhibit long characteristic relaxation times that lead to a variety of elastic instabilities in various flow geometries [12], [13]. It is now generally accepted that, in addition to particular instabilities, chaotic flows can also occur i.e. irregular flows that exhibit a range of time and length scales. Such flow behaviour is referred to as elastic turbulence [14], [15] due to the similarity of certain features of the flow to inertial turbulence.   Studies of elastic turbulence are most commonly made with Boger fluids [16] or fluids with properties approaching those of an ideal Boger fluid, i.e. where elastic effects can be separated from viscous effects in viscoelastic flows. In general this means dilute systems. Whereas the use of Boger systems brings clarity to the essential behaviours being studied, additional features due to inter-molecular interactions are largely absent. Conversely similar instabilities in polymer melts have received significant attention due to their implications for polymer processing technologies. A number of increasingly complex constitutive relations have been proposed and studied. One advanced, yet computationally tractable model, is the Rolie-Poly model [17].   The model is a single mode approximation to the Graham-Likhtman and Milner-McLeish model [18] which encompasses the physical molecular processes of reptation, convective constraint release (CCR), chain stretch and retraction. The resulting constitutive relation requires four parameters: τ_{rep} the reptation time, τ_R the Rouse relaxation time, β^* the CCR parameter and δ a parameter used to fit the simplified model to the full model. Hence within this model one can expect processes dominated by each of the two timescales: (i) shear thinning and linear elastic behaviour, i.e. orientational relaxation, at a shear-rate of order $1/\tau_{rep}$ and, (ii) non-linear elastic effects, i.e. stretch relaxation, at deformation rates of order $1/\tau_R$.

In the present study we investigate experimentally the flow of high molecular weight (3.5 – 35 MDa) partially hydrolysed poly-acrylamides (HPAM) via flows in porous media (rock cores and microfluidic networks (micromodels)) and in conventional shear rheometry. We have observed that for flow in porous structures, on increasing the apparent shear-rate the flow becomes unstable and

transitions from steady laminar flow to a flow varying randomly in space and time, i.e. elastic turbulence. We find the surprising result that the onset of elastic turbulence is concentration independent for concentrations above approximately $10c*$. This independence is in contrast to an expected strong concentration dependence of relaxation times for these systems and leads to significant ramifications in the choice of polymer formulation for practical use.

In a future study we will focus on the detailed interaction of the aqueous phase flow turbulence described here, with oil trapped in the porous medium.

We first describe the experimental materials and procedures in section 2. Subsequently in section 3 we present results beginning with a brief description of the data analysis. In section 3.2 we show flow measurements for a range of polymer solution concentrations and separately for a range of mean polymer molecular weights. In section 3.3 we briefly demonstrate that the observed flow thickening in porous flow is associated with elastic turbulence and in section 3.4 that the observed flow thickening due to elastic turbulence onset can also be observed in a cone-and-plate rheometer and moreover that the scalings observed in porous flow are also observed in this rheometer configuration. In section 3.5 we show the collapse of the porous flow data when scaled with appropriate rheometer measurements. We discuss these results in section 4 and finally conclude in section 5.

2   Experimental

2.1   Polymer solutions

Viscoelastic polymer solutions were prepared using partially hydrolysed polyacrylamides (HPAM) supplied by SNF Floerger covering a range of mean molecular weight (Table 1). In all cases we chose to work with an ionic strength of 74 mM to coincide with a particular oil field aquifer example. HPAM is a polyelectrolyte and so the ionic strength is expected to affect the behaviour of the molecule in solution. The degree of screening of the polymer charge may be assessed by comparing the ionisable monomer number density concentration, c, with $2Ac_s$ [19], where A is the number of monomers between uncondensed charges and c_s is the salt concentration. Here A is ≈ 2 for the range of polymers except 6040S where it is 1.5. For our solutions a typical concentration is 0.12wt% corresponding to (1.2/71) 17mM of monomers. Hence $c << 2Ac_s$ (i.e. 17 << 2*2*78) and we expect the salt ions to screen the coulomb interactions between monomers. Hence we expect the molecule to behave to first order as a neutral polymer in a good solvent. We indeed see low-shear viscosity $\eta(0) \sim c^n$ with n between 3 and 3.5 for our systems (Figure 3c), rather than the low-salt limit for polyelectrolytes ($\eta(0) \sim c^{3/2}$). Thus at this ionic strength, we expect that the entanglement concentration $c_e \approx 10c*$, as for a neutral polymer [19].

HPAM Material	MW (MDa)	$c*$ (wt %)	Hydrolysis (mol%)
3130S	3.6	~0.048	30
3230S	6	~ 0.025	30
3330S	10	~0.016	30
3430S	11	~ 0.014	30
3530S	16	~0.011	30
3630S	18-20	0.008	30
6040S	30-36	~0.004	40

Table 1 Properties of SNF Floerger, partially hydrolysed polyacrylamides used in this study. $c*$ for 3630S was measured via viscometry, values for the other molecular weights were inferred from extrapolated viscosity-concentration measurements.

Solutions were prepared to explore a range of concentrations (all entangled). Further solutions were prepared to explore the range of mean molecular weight available. In this latter case

we chose to vary the concentration such that the low shear viscosity of the sequence of solutions remained constant. All solutions were fully hydrated by rolling for 24 hours before being filtered to remove particulates and undispersed polymer. To prevent biological or oxidative degradation of the polymer, preservative (15 wt% isopropanol, 7.5 wt% thiourea and 77.5wt% water) was added to each stock solution at mass two-thirds that of the dry mass of the polymer.

2.2   Shear rheology

All measurements were made with a Malvern Gemini NanoHR rheometer with a 40 mm diameter cone-plate measuring geometry. The majority of measurements were made with a 4° cone and a few with a 1° cone, which enabled access to stable flow at higher shear. The measurements throughout this work were at 20°C. Flow-curve measurements of viscosity η were generally made in stress-control mode. The range of shear depended on the sample in question but was selected so as to enable the determination of the low-shear limiting viscosity $\eta(0)$ and avoid ejection of fluid at high shear. On increasing shear, the flow curves were well described by a plateau at low shear, then a thinning region and finally a region of apparent thickening during which flow was unstable (the noise/signal ratio increased, the fluid appeared to pulse). In this region of unstable flow, the ratio of the first normal stress difference to the shear stress was constant ($N_1/\sigma \approx 50$ for a 4° cone and ≈ 100 for a 1° cone).

The plateau and thinning behaviour were well described by the Carreau-Yasuda model,

$$\eta(\dot{\gamma}) = \left[\eta(0) - \eta(\infty)\right]\left[1 + \left(\lambda_{CY}\dot{\gamma}\right)^a\right]^{\frac{n-1}{a}} + \eta(\infty) \tag{1}$$

where λ_{CY} is the relaxation time, n the power-law index and a a parameter that describes the transition from Newtonian to shear-thinning behaviour. The limiting high-shear viscosity $\eta(\infty)$ is set to zero unless the data clearly indicate a reduction in the rate of thinning (as would be the case at high rates accessible with a 1° cone).

2.3   Flow through porous rock

A cylindrical plug of rock (a core of length 50 mm and diameter 38 mm) cut from a Bentheimer sample was first characterised by measurement of permeability and porosity independently using a conventional gas permeameter (ErgoTech). The Bentheimer formation is a relatively homogeneous outcrop sandstone which is naturally water-wet. For our samples the permeability is $k \approx 3100$mD ($\approx 3.0\mu m^2$, 1Darcy $= 9.869 \times 10^{-13} m^2$) and the porosity $\phi \approx 0.23$. The core plug was placed in an evacuated chamber. A degassed sample of the 74 mM brine was then introduced to the evacuated chamber thereby filling the rock and ensuring no trapped gases. The solution-filled core plug was transferred to the core holder and confining pressure of 1200psi (1psi = 6.85kPa) applied to the confining sleeve to prevent flow of liquid around the core.

The flow of liquids through porous rock materials is investigated routinely using a "core-flood" apparatus in which liquid is flowed in a controlled rate through a plug of rock. We have constructed our measurement system based on a standard core holder (E.P.S. Coresystems) as shown schematically in Figure 1. The liquid is supplied by a high-pressure syringe pump (Teledyne ISCO) to the inlet distribution platen of the core holder. Pressure at the inlet face is measured by one of four pressure transducers (Keller PX33 series) thereby enabling the measurements to cover a wide dynamic range (0.1 psi to 450 psi). The outlet platen flows to a collection port and a pressure transducer measures the pressure at the core face. The average linear pressure gradient along the core is thereby simply determined as a function of imposed flow rate. Note that the purpose of the platen is to distribute the flowing liquid uniformly across the face of the core such that the porous flow is predominantly 1D, i.e. along the core only. To ensure that there are no effects on the pressure measurement due to redistribution of the flow near the inlet, it is common to provide pressure taps along the core. For this core holder, the core is too short to allow for this arrangement and (non-flowing) end taps are used instead. Whereas correction for the end effect may be made, in the data presented no allowance is estimated and the data presented without modification.
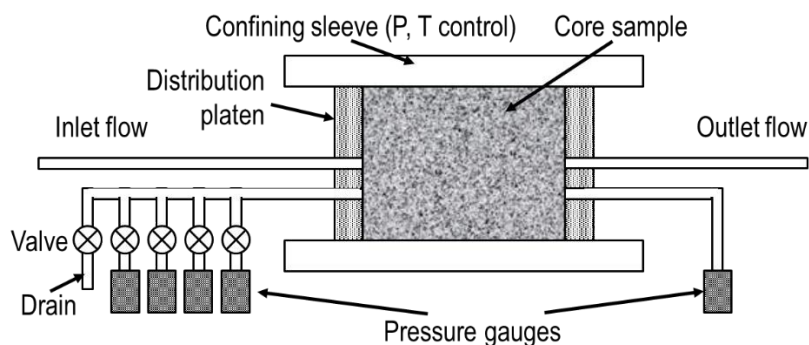
Figure 1 Core-flood apparatus. Inlet flow is supplied by a high-pressure syringe pump, outlet flow is to atmosphere. Inlet and outlet pressure gauges cover a range from 0 to 30bar. The rock core sample is confined by a flexible sleeve and pressurised to 1200psi.

2.4   Particle Tracking Velocimetry (PTV) in a microfluidic network

Core floods allow macroscopic flow parameters to be measured for a range of liquids but provide little direct information regarding the microscopic details of the flow. For this purpose we have used microfluidic approximations of a pore structure (micromodels) as shown in Figure 2. This lattice comprises a 2D net of channels of 100μm depth. Pores are 200μm squares connected in a square net to each other by pore throats of width randomly distributed about 75μm with a range from 50μm to 150μm. The square net is oriented at 45° to the mean flow. The inlet is a single channel that feeds a wide distribution region coupled to the porous net by a set of parallel channels. This arrangement approximates a uniform inlet-flow rate. Channels have been fabricated in SU8 on a PMMA support material (Epigem Ltd.). The SU8 surfaces are hydrophobic in nature (contact angle for deionised water in air $\theta \approx 81°$) and are used as supplied. In order to fill the device geometry without gas bubbles a pre-flush with methanol is used, which is subsequently flushed with the brine to be used in the particular experiment. The microfluidic geometry has channels approximately 2x the pore-entry throat diameter of the rock (38.8μm, determined by mercury intrusion porosimetry) described above. The design hence has comparable length-scales to that in the rock whilst preserving ease of manufacture.

The network has two side channels across which is placed either a differential pressure transducer (Honeywell 24PC series) or a pair of gauge pressure transducers (LabSmith). Thus macroscopic measurements (flow rate and pressure gradient) directly comparable to the core flood arrangement can be made whilst also performing pore-scale imaging measurements.
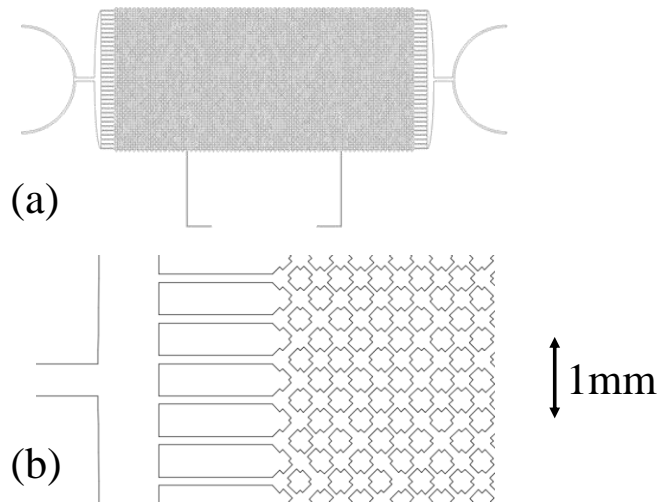
Figure 2 Microfluidic geometry (MM2). (a) Complete structure, channel depth is 100μm. Two pressure taps are provided along the edge of the device. (b) Close-up of section near the inlet of the model; pores are 200μm square and pore-throats are randomly distributed about 75μm width.

Detailed flow velocity measurements are made by seeding the flow with 1μm polystyrene particles (Sigma-Aldrich) and capturing high-speed images (Provision M1) via a moderately high numerical aperture lens system (Navitar). Analysis of the image sequences (LabView) provide spatial liquid velocity measurements (PTV [20]). The lens used gives a depth of focus approximately 1/3 the channel depth and thus velocity measurements are plane projections of the 3D velocity vector within the middle of each channel.

3 Results

3.1 Analysis background

The flow of liquids in small channels is typically dominated by viscous and capillary forces. This situation is characterised by a small Reynolds number, Re, for such flows. As such, inertial forces can be ignored and the result is the well-known Stokes equation for creeping flow. Such flows are laminar and steady. For a random porous medium, flow is usually described by the Darcy equation,

$$Q = -A\frac{k}{\eta}\nabla P \qquad (2)$$

where Q is the volumetric flow rate through a cross sectional area A of the porous medium, k is the permeability, η the viscosity and ∇P the pressure gradient. This equation originated as an empirical correlation [21] but can be justified for Newtonian liquids on the basis of Stokes equation [1]. There have been a number of studies seeking to extend the foundation of Darcy's equation to be applicable to non-Newtonian flow [2] [22] [23]. Results for power-law fluids indicate that effective rheograms can be obtained by inverting equation (2) for viscosity and taking the apparent shear-rate and viscosity as respectively,

$$\dot{\gamma} = \alpha\frac{Q}{A\sqrt{k\phi}}; \qquad \eta(\dot{\gamma}) = -\frac{Ak\nabla P}{Q} \qquad (3)$$

with ϕ the porosity and α a constant factor allowing the porous flow rheogram [24] to be overlaid with the bulk measured rheogram. It should be noted that the flow in a porous medium is not expected to be pure shear, so it is perhaps more correct to use "apparent deformation rate". For the viscoelastic liquids under consideration here, this distinction is important since we expect a significant extensional contribution to flow at the pore scale. Nevertheless, in what follows we chose to present our porous pressure/flow-rate data as apparent rheograms. For the rock-core flow data presented in this work,

the permeability estimated from flow of brine has been used to calculate both apparent shear rate (using a value of $\alpha=1$) and apparent viscosity.

Instabilities in the flow of viscoelastic fluids have been known and studied for very many years. In 2000 Groisman and Steinberg [14] coined the term "elastic turbulence" to describe a widely observed chaotic instability. Such instabilities are characterised as exhibiting fluctuations in flow velocity over a broad range of spatial and temporal frequencies up to a relatively sharp power-law cut-off above a threshold frequency. Elastic turbulence has been observed in a number of situations [25], including microchannel flow [26], and has been proposed as a method of mixing within microfluidic devices [25].

McKinley et al. [27], [28] have proposed a dimensionless parameter, M, to characterise the onset of purely elastic flow instabilities,

$$M = \sqrt{Wi.De} \qquad (4)$$

with Wi the Weissenberg number and De the Deborah number. Linear-stability analysis for a cone-and-plate rheometer geometry [29] shows that the flow of a viscoelastic fluid becomes unstable when $M \geq \sqrt{21.17}$, where M is defined for this geometry as,

$$M = \frac{\lambda_{PM}\omega}{\sqrt{\theta_0}} \qquad (5)$$

and where ω is the rate of rotation of the cone, θ_0 the angle between the cone and the plate and where λ_{PM} is a characteristic relaxation time (we use suffix PM for Pakdel-McKinley to distinguish this time) of the viscoelastic fluid.

Whereas M was introduced to describe the point at which linear stability is lost and not necessarily the transition to elastic turbulence, since in our experiments we observe laminar flow transitioning directly to elastic turbulence, we follow Zilz [26] and take an M to describe loss of stability and the onset of turbulence. Thus, in considering viscoelastic flow in a porous medium we should also expect elastic turbulence for M greater than a critical value, M_{crit}. If we assume equation (4) to hold and take the usual definitions for Weissenberg and Deborah numbers,

$$Wi = \lambda\dot{\gamma}; \quad De = \lambda\frac{U}{L} \qquad (6)$$

with $\dot{\gamma}$ the shear rate, U a characteristic pore velocity and L a characteristic flow length. Then, taking the shear length scale to be a, the pore throat radius,

$$M = \sqrt{Wi.De} = Wi\left(\frac{a}{L}\right)^{1/2} \qquad (7)$$

and using equation (3),

$$M = \lambda\left(\frac{\alpha Q}{A\sqrt{k\phi}}\right)\left(\frac{a}{L}\right)^{1/2} \qquad (8)$$

Note McKinley et $al.$ define the lengthscale L as the radius of curvature of a streamline within the flow, which might correspond to a grain size within a rock structure (hence $a/L \approx 0.27$ for Bentheimer [30]). However, here we merely assume a lengthscale related to the pore structure exists but investigate no further. Thus at the onset of elastic turbulence $\lambda \propto (1/Q)$ and therefore that the onset of elastic turbulence for a particular porous structure characterises a liquid relaxation time. Note further that, rearranging,

$$Q_{crit} \propto \left(\frac{k\phi}{\lambda^2}\right)^{1/2} \qquad (9)$$

i.e. the critical flow rate for onset of elastic turbulence, Q_{crit}, may be estimated based on the relaxation time and the characteristic rock properties of permeability and porosity.

3.2 Flow thickening: dependence on concentration and molecular weight

The macroscopic behaviour of polymer solutions when flowed through rock cores have been reported a number of times, e.g. [11], [31], [32]. For solutions of flexible polymers, when the pressure – flow rate data are presented as described by equation (3), the apparent flow curve follows that measured in a rheometer until a critical deformation rate, above which the material flowing in the rock apparently flow thickens. The observation of thickening is in contrast to the equivalent measurement in simple shear using a standard rheometer geometry. In a conventional rheometer study no thickening is observed at shear rates equivalent to the deformation rate in the rock core.

A particular interpretation of these observations is to invoke the onset of a strong extensional viscosity component. Whereas this is a reasonable argument, it fails to explain the recently reported multiphase desaturation data [11].[1] Thus, whereas additional viscous dissipation due to extensional flows is likely, it is the *additional* dissipation route due to elastic turbulence that we believe to be of primary importance.

In this section of the paper, we compare the flow behaviour of HPAM solutions in a conventional rheometer with cone-and-plate geometries and in in a sandstone rock core. We will first vary the polymer concentration at a given molecular weight and then vary the molecular weight at a given low-shear viscosity. The data will be used to determine characteristic relaxation times for different processes and it will be clear that the behaviour describing the onset of thickening in porous flow is different from that describing the linear relaxation properties in shear flow.

In Figure 3 we show data for the *highest molecular weight material (6040S, 30-35MDa) at a series of concentrations* that give rise to $\eta(0)$ values ranging from approximately 2 mPa.s to 30 Pa.s. Figure 3(a) shows flow curves for different polymer concentrations measured in the rheometer (filled points) and derived from rock-sample flow (open points) using equation (3). The onset of flow thickening in the rock is constant, at approximately $1s^{-1}$, independent of concentration. The concentration independence of flow thickening has been reported previously by Seright [32] for concentrations 2.5-8×$c*$with 18-20 MDa HPAM at a higher ionic strength. The flow data from the rock sample show a flattening at the highest apparent shear-rates. Subsequent measurement of low-shear viscosity and analysis of extensional viscometer data (CaBER) using solutions that were exposed to such rates demonstrate that some degradation had occurred. The experimental procedure was such that measurements at $Q > Q_{crit}$ were always made on stepwise increasing rate and care was taken to ensure no mechanically degraded polymer was the in the core during low-rate measurement. In Figure 3(b) are shown the shear rheometry data fitted, from low-shear plateau to the end of the shear-thinning region, using a Carreau-Yasuda model. In Figure 3(c) are plotted the low-shear viscosity, $\eta(0)$, and relaxation time, λ_{osc}, from a frequency sweep at small amplitude ($1/\omega$ where $G'=G''$). In addition, in Figure 3(c) are plotted the characteristic times for the onset of the observed thickening, λ_{core}, derived from the data in Figure 3(a), as described later.

---

[1] The extensional viscosity for the solutions studied here increases with polymer concentration, while the onset of apparent thickening we will demonstrate to be independent of concentration for these solutions. The filament break-up time in CaBER measurements was found to be proportional to polymer concentration.
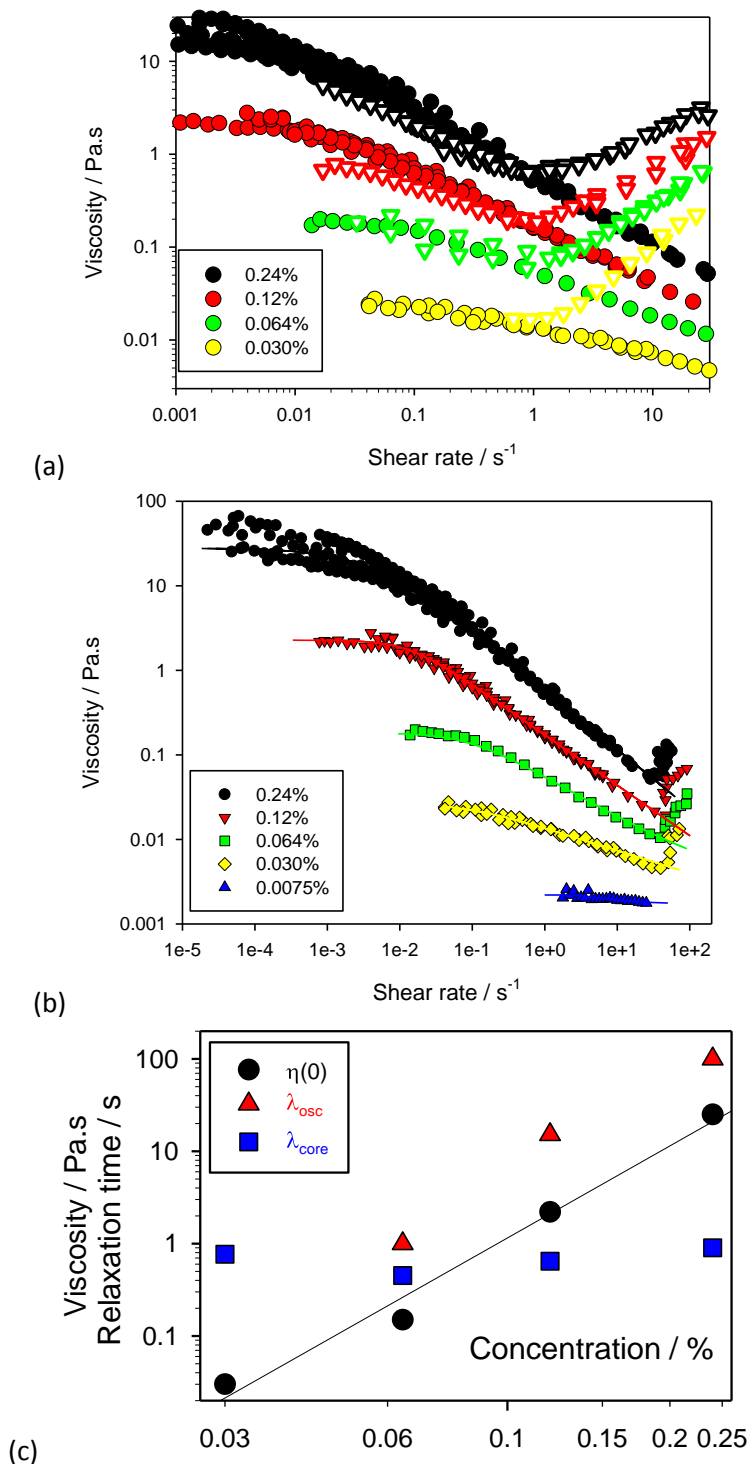
(a)

(b)

(c)

Figure 3 Scaling as a *function of concentration* for 30-35 MDa HPAM 6040S. (a) Open symbols - apparent flow curves for a range of 30-35MDa HPAM concentrations with constant ionic strength derived using equation (3); filled symbols - the rheometer data from (b) (b) Rheometric flow curves with low-shear ($\leq 10s^{-1}$) part of the curve fitted using the Carreau-Yasuda model, and (c) Characteristic relaxation time, λ_{osc}, and low-shear viscosity $\eta(0)$, and apparent flow thickening, λ_{core}, plotted as a function of concentration.

In Figure 4 are plotted similar data, but here we follow the behaviour of solutions of HPAMs of *different mean MW* prepared at concentrations with a *constant low-shear viscosity of 2Pas* . In

Figure 4(a) are shown apparent flow curves generated from rock-core measurements; as molecular weight increases, the onset of flow thickening translates to lower apparent shear-rate. Figure 4(b) shows rheometer flow curves for the same set of polymer solutions as were used for the core-flow experiments. These data have again been fitted using a Carreau-Yasuda model. Last, in Figure 4(c) four characteristic times are plotted: λ_{osc}, derived as the crossing point of G' and G'' in a low-amplitude oscillatory frequency sweep (see Appendix); λ_{CY}, the characteristic time describing the transition to shear thinning in the rheometer flow curve; λ_{core}, the characteristic time for the onset of flow thickening derived from Figure 4(a); and, λ_{PM}, the characteristic time derived from the onset of thickening in the cone-and-plate rheometry (see below).
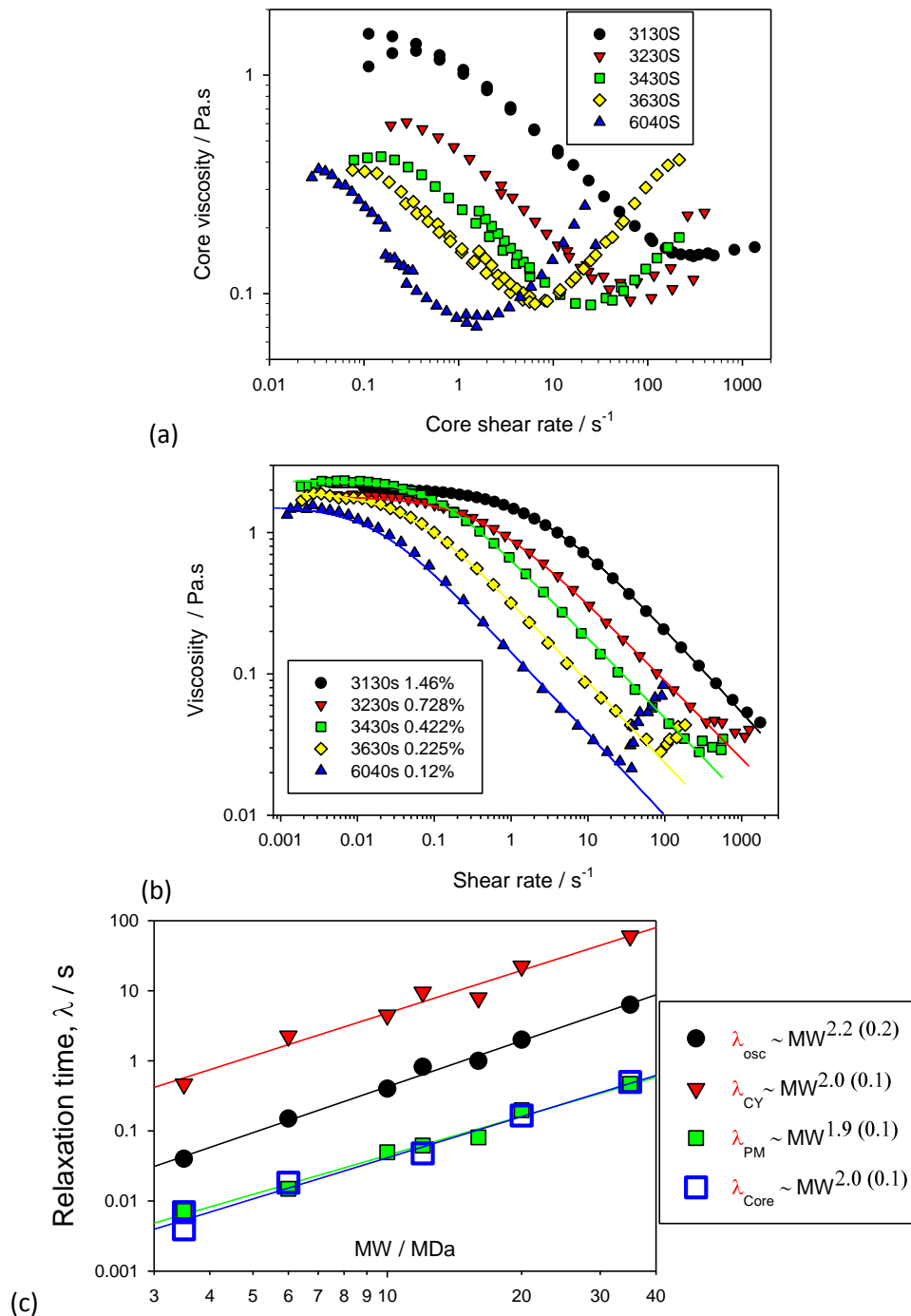
(a)

(b)

(c)

Figure 4 *Scaling as a function of MW* for $\eta(0)$ 2 Pa.s solutions. (a) Apparent flow curves for a range of molecular weight HPAM in a rock core, (b) rheometric flow curves with low shear part of the curve fitted using the Carreau-Yasuda model, and (c) characteristic times derived from various measurements: oscillation measurement λ_{OSC} (see Appendix), from the Carreau-Yasuda fit in (b) λ_{CY}, from the observed upturn in (b) (see below) using equation (5) λ_{PM}, and from the position of the apparent flow thickening in (a), λ_{core}. All characteristic times scale approximately as MW^2 for this set of data. Note concentration varies across the set.

It is instructive to plot datasets such as those shown in Figure 3 and Figure 4 in such a way as to demonstrate the flow thickening apparent in the core-flow measurements. We choose to plot the apparent viscosity derived from the core measurement divided by the Carreau-Yasuda curve obtained from fitting the corresponding rheometer flow curves. Such a plot is equivalent to plotting the excess

pressure drop in the core divided by that expected based on a Darcy approach using the Carreau-Yasuda model fluid (Note this is an equivalent plot to that used by Burghelea *et al* [33] for a Boger fluid, their fig. 2, but here applied to a shear thinning fluid). The result is shown in Figure 5a. In Figure 5b we take the onset of thickening ($1/\lambda_{core}$ obtained by fitting an inverse Carreau-Yasuda function to the data shown in Figure 5a) from these data and plot against the low shear viscosity of each solution. We see now for HPAMs of a series of molecular weights, that the onset of flow thickening is approximately concentration independent. Data are also included for a solution of the stiff polymer xanthan, which has similar a similar $\eta(0)$ to, and slightly shorter Carreau-Yasuda relaxation times than, the 18 MDa HPAM 3630S of the same concentration. Any apparent flow thickening for xanthan occurs at a very much higher rate than for even the lowest MW HPAM studied here.
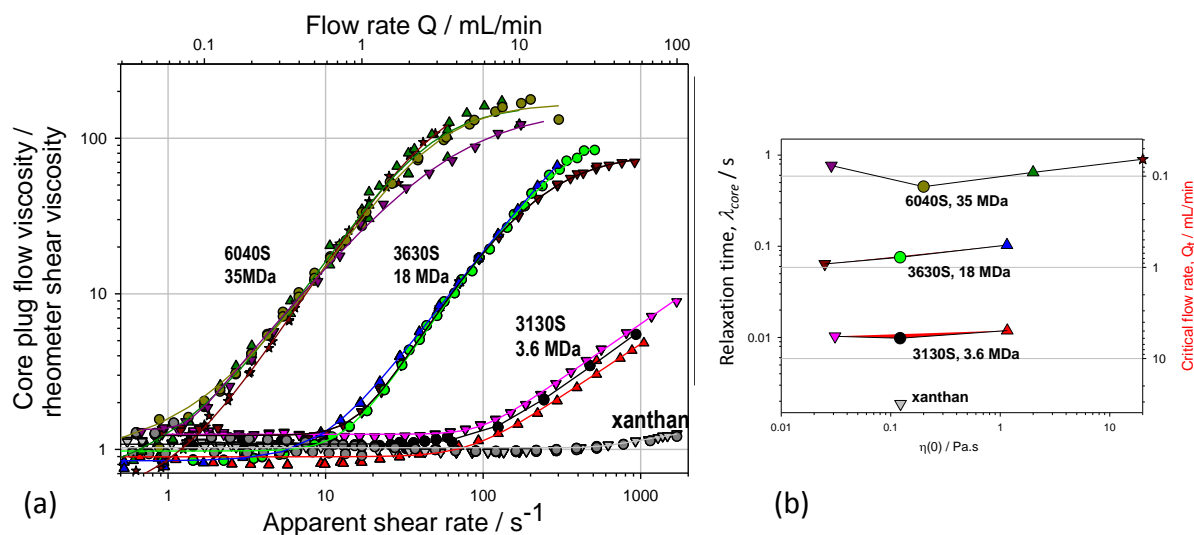

Figure 5 (a) Ratio of apparent viscosity derived from porous flow measurement divided by the Carreau-Yasuda flow curve fitted to rheometer measurement. A range of solution molecular weight and concentration are plotted. (b) The characteristic time, λ_{core}, taken as the inverse shear rate for thickening seen in (a) is plotted against the solution low shear viscosity.

The data presented in Figure 3, Figure 4 and Figure 5 illustrate two systematic trends concerning the observed onset of apparent thickening as a function of apparent shear rate, $\dot{\gamma}_{onset}$:

(i)   Figure 3 and 5: The onset is *independent of polymer concentration* provided the concentration is greater than about $8c^*$. Most authors [31] [34] assume that the observed onset of thickening is related to the linear elasticity of the polymeric solution. However, if that were the case then the onset would be a strong function of concentration: clearly it is not.

(ii)   Figure 4 and 5: The onset is approximately *inversely proportional to the square of the molecular weight*, $1/\dot{\gamma}_{onset} = \lambda_{core} \sim MW^2$. Since the concentration is varying over this series of solutions but the onset is observed to be approximately independent of concentration, this is the molecular weight scaling for any particular concentration and is different from that of the Carreau-Yasuda time for thinning, $\lambda_{CY} \sim MW^3$ (see below).

These two observations demonstrate that the apparent thickening is not simply related to the linear viscoelasticity of the polymer solutions (see also Figure 8). Rather, there is a characteristic time that behaves as a function of concentration and molecular weight as would be expected for a single molecule. We return to explore this further in the discussion section below.

3.3   Flow thickening: correlation with elastic turbulence

An increased pressure gradient in single-phase flow of viscoelastic solutions, interpretable as flow thickening, has been shown to coincide with the onset of elastic turbulence in single curvilinear

channels [26], in non-uniform single channels [35] and in porous media [11]. The observed fluctuation onset in microfluidic devices (micromodels) for the solutions used herein also coincide with the observed flow thickening.

In Figure 6 we show for 0.12wt% 18MDa HPAM (3630S) example streakline images at flow rates below and above the transition to elastic turbulence. For the lower flow rate we see simple laminar flow whereas for the higher flow rate we see crossing streaklines. Furthermore where we see crossing streaklines, the image sequence shows frames where particles at the same apparent position are travelling in markedly different directions which we interpret as a complex three dimensional flow. Moreover the velocity at a particular position fluctuates in time. Since the onset of fluctuations is independent of polymer concentration, it is not appropriate to use a Weissenberg number defined with a characteristic time taken from linear-viscoelastic measurements as such a time is strongly dependent on concentration. However, using a characteristic time as derived from the rheometer measurement described below we find Wi = 0.35 and 3.5 respectively which give values of M, estimated using equation(7), of M=0.16 and 1.6 respectively. Note that the onset of fluctuations is observed for a flow rate of about 9μl/min [11], at which point $Wi_{crit} \approx 1.04$ and, taking a = 37.5μm and L = 176μm (pore throat half width and the radius of an inscribed circle =500/2√2 respectively), $M = M_{crit} \approx 0.48$.
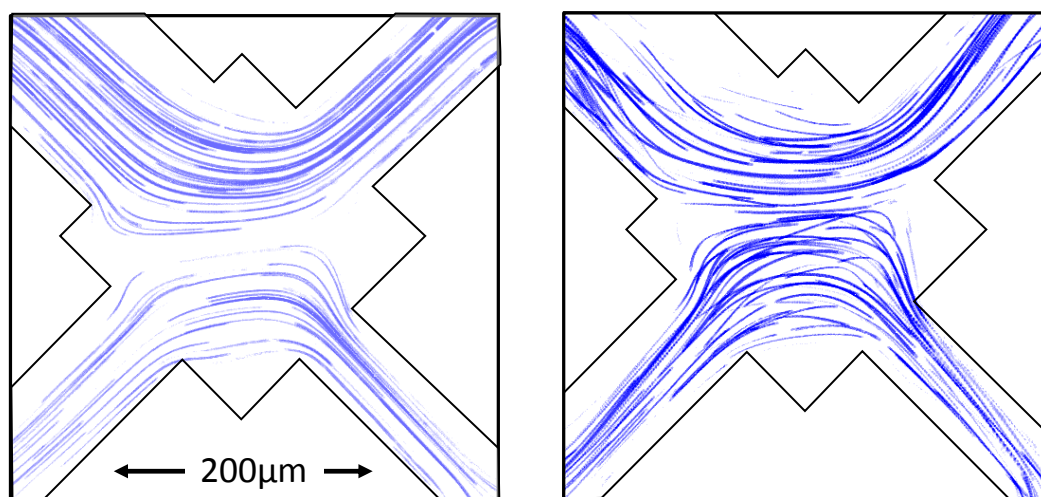

Figure 6 False colour streakline photographs (inverted dark-field imaging, with blue particle traces) illustrating onset of elastic turbulence for a 0.12wt% solution of 3630S. Left: Q = 3μL/min, M=√(De.Wi) = 0.16 showing steady laminar streaklines. Right: Q = 30μL/min, M=1.6 showing unsteady multiple crossing streaklines. [$M_{crit} \approx 0.48$ at threshold].

The imaging of particles within the microfluidic structure further enables us to extract local velocities and thereby to quantify the onset of elastic turbulence [11]. In Figure 7 we plot the velocity fluctuation amplitude observed in 1s within a 100μm x 100μm region at the centre of a pore for three concentrations of 18MDa HPAM (3630S). It has been observed previously that the probability distribution function of velocity becomes asymmetric and non-gaussian [15]; in our case significantly so. We therefore choose to plot the width of this distribution rather than a standard deviation. It is clear that the fluctuation onset is at a constant flow rate to within the scatter of the measurements. Note that linear viscoelastic relaxation time varies by more than an order of magnitude over this concentration range as does the low-shear viscosity of the solutions (Figure 10).
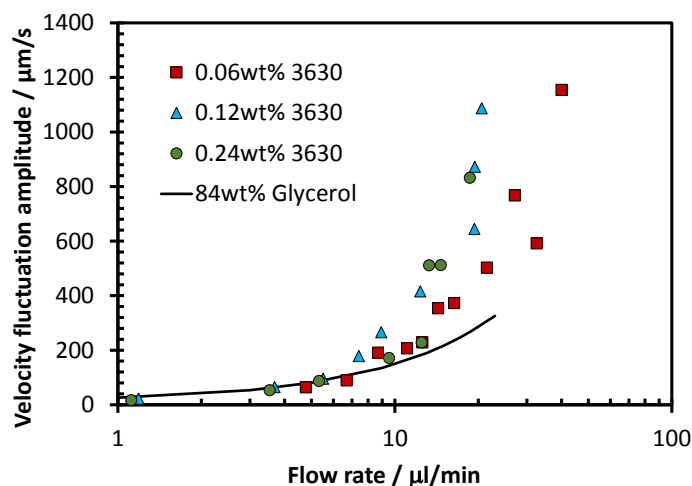
Figure 7 Microfluidic PTV fluctuation analysis. Here we plot the peak-to-peak amplitude of velocity fluctuations in a central region of a pore for HPAM compared to that observed with 84wt% glycerol ($\approx$74mPa.s). Flow fluctuations depart from the Newtonian case (i.e. glycerol) at flow rates between about 6μL/min and 10μL/min. Hence, the onset is independent of polymer concentration and coincident with apparent flow thickening within experimental error [11].

3.4   Flow thickening: corresponding observation in a rheometer

The HPAM polymers used in our experiments have been characterised in conventional shear (Figure 3(b) and Figure 4(b)). In this section, we determine characteristic exponents describing the concentration and MW dependence of the standard shear behaviour (viscosity, onset of shear thinning). These materials, despite being commercial polydisperse systems, follow the scaling expected for linear viscoelastic behaviour, which is very different from that we determine for the onset of thickening. We then describe the onset of unstable flow at high shear in the cone-and-plate geometry and find its scaling similar to that of the onset of thickening at high flow rates in rocks. These findings are in contrast to the assumption made by other workers that the linear-viscoelastic scaling defines the thickening behaviour [31], [34].

For the set of experiments shown in Figure 4(b) concentrations were adjusted to obtain comparable low shear viscosities of approximately 2Pas. In all cases the concentrations are *c$\geq$10c** and hence are expected to be entangled. In Figure 8 we re-plot the Carreau-Yasuda characteristic time together with the solution concentration that gives the target low-shear viscosity. There is clearly a power-law dependence for each of these parameters.
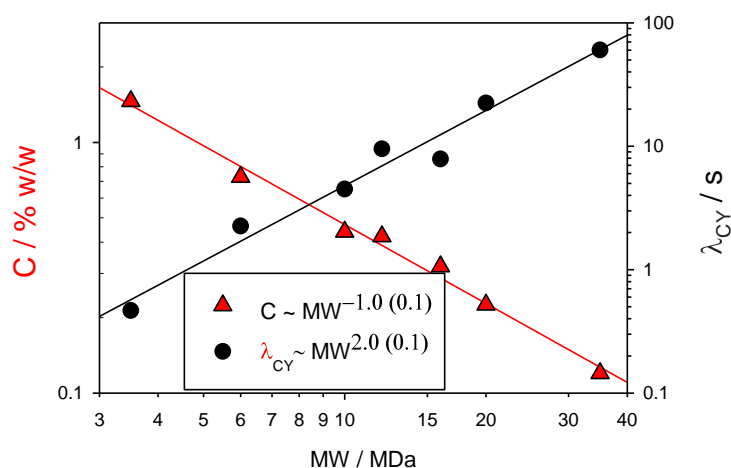
Figure 8. Log-log plots of Carreau-Yasuda relaxation times and low shear viscosities, $\eta(0)$, taken from fits to the data in Figure 4. In each case concentration was been adjusted such that the low-shear viscosity is approximately 2 Pas. The power law behaviour corresponds to entangled systems with scaling exponent $\nu\approx2/3$, indicating behaviours close to, but not quite, that of a neutral polymer in a good solvent [36].

Assuming that our solutions are indeed in the semi-dilute-entangled regime, then we might reasonably expect the low-shear viscosity to scale as [36],

$$\eta(0) - \eta_s \propto N^3 \cdot c^{3/(3\nu-1)} \tag{10}$$

If we choose a series of molecular weights and concentrations such that $\eta(0)-\eta_s \approx 2$ Pa.s is constant, as in Figure 8, then we should therefore find $c \propto N^{-(3\nu-1)}$. Taking this scaling and noting the number of Kuhn monomers $N \propto MW$, our data implies $\nu\approx2/3$, a value close to that expected of a neutral polymer in a good solvent (0.588) and appropriate for an incompletely screened polyelectrolyte. This exponent value compares well with that calculated for a polyelectrolyte system ([37] figure 4) with a Debye length appropriate to characterise our systems. Using ν=2/3, the reptation time, τ_{rep}, for this same set of experiments should scale as

$$\tau_{rep} \propto N^3 \cdot c^{3(1-\nu)(3\nu-1)} \propto N^3 \cdot c^1 \tag{11}$$

The reptation time here does not take account of the polydispersity expected for these samples but nevertheless should correlate with the characteristic time encompassed in the Carreau-Yasuda constitutive relation. Since for this set of experiments we have already determined that $c \propto 1/N$, then from equation (11) $\tau_{rep} \propto N^2$ which, if we associate λ_{CY} with τ_{rep}, is expected as indeed we observe [36].

The HPAM polymer series at the concentrations used here ($\eta(0)$ from 0.02 to 20 Pa.s) therefore behave as we would expect of semi-dilute entangled systems in simple shear. Further, they are sufficiently screened to behave more like neutral polymers in a good solvent than as pure polyelectrolyte systems.

The onset of an elastic instability was previously observed in a cone-and-plate rheometer configuration [27]. The linear-stability analysis by Olagunju [29] led to an onset criterion we reproduce as equation (5). In our experiments there is an anomalous increase in viscosity above a critical shear rate associated with unstable flow and strongly fluctuating stress (Figure 9). This upturn in the cone-and-plate measurement is easily confused with the conventionally known inertial instabilities associated with this geometry (i.e. Taylor vortices). However, if an inertial instability, it should be suppressed by increasing the fluid viscosity, which is clearly not the case (Figure 10). (Note: we do see the inertial instability for simple shear-thinning fluids at sufficiently high rotation rates.) Comparing the data in Figure 9(a) with those shown already in Figure 4, the corresponding upturn for each molecular weight solution is apparent. In Figure 9(b) are shown data illustrating the transition to unstable flow using 0.225% 3630S as example. The standard flow curves describe steps increasing in stress at ten steps per decade with 20 s at each stress; these data are shown as symbols. The onset of thickening (circles) occurs at 92 s^{-1} while on decreasing shear (triangles) the viscosity is higher until approximately 40 s^{-1}. Two experiments continuously ramping up and then down in shear stress between 0.1 and 10 Pa were carried out over 3333 s and 333 s, with an "instantaneous" viscosity value recorded each second. The onset of thickening occurs from lower rate (74 s^{-1}) for the slow ramp than for the faster ramp (145 s^{-1}) – values spanning that obtained with stepped stress. At shear above these transitions the viscosity data are very noisy. On decreasing shear, the noise disappears and the viscosity returns to steady shear thinning at 45 s^{-1} for both the fast and the slow sweep, very similar to the value obtained with step shear. Thus there is hysteresis in the observed transition, which may indicate a sub-critical instability.
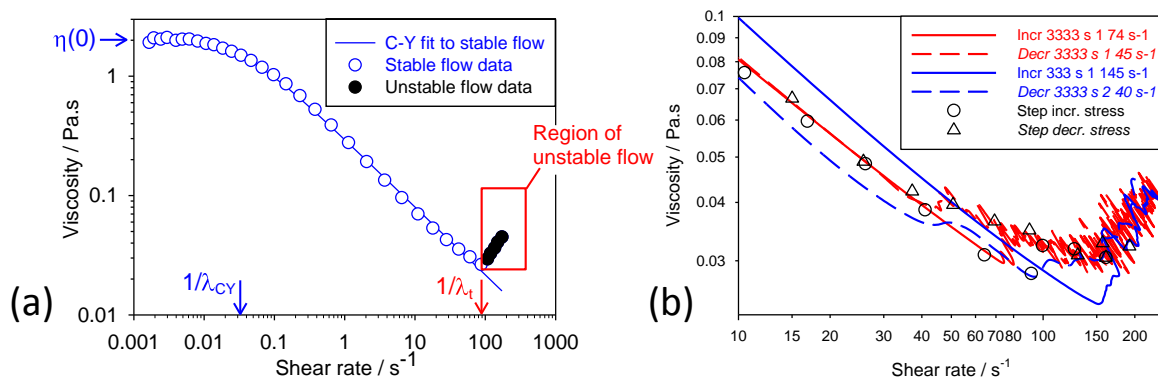
Figure 9 (a) Unstable flow in the cone and plate rheometer, definition of terms. On increasing shear rate we first see a low-shear Newtonian plateau, viscosity $\eta(0)$. Above a shear rate characterised by a relaxation time λ_{CY}, the solution shear thins. Finally, above a higher critical shear rate, $\dot{\gamma}_t$, the measured viscosity increases. A characteristic relaxation time, λ_{PM}, can be derived from $\dot{\gamma}_t$ using equation (5). (b) The transition to unstable flow illustrated using 0.225% 3630S as example, see text for description.

Detailed flow curves, obtained with the cone-and-plate rheometer, for three concentrations of 18MDa HPAM (3630S) are shown in Figure 10. Two cone angles were used as indicated in the figure. The data show that for each cone angle the onset of unstable flow is close to independent of concentration. The fitted Carreau-Yasuda relaxation time (λ_{CY}), however, varies by about a factor of 20. When plotted against $1/\lambda = \omega/\sqrt{21.17\theta_0}$ from equation (5) (Figure 10b), the onset (=$1/\lambda_{PM}$) implies a characteristic time of approximately 0.17s. Thus, using the cone-and-plate geometry together with the interpretation provided by Olagunju [29], we have access to a characteristic time independent of the porous-flow experiment. Using this time we obtain a Weissenberg number of 0.35 and 3.5 for the flows shown in Figure 6.
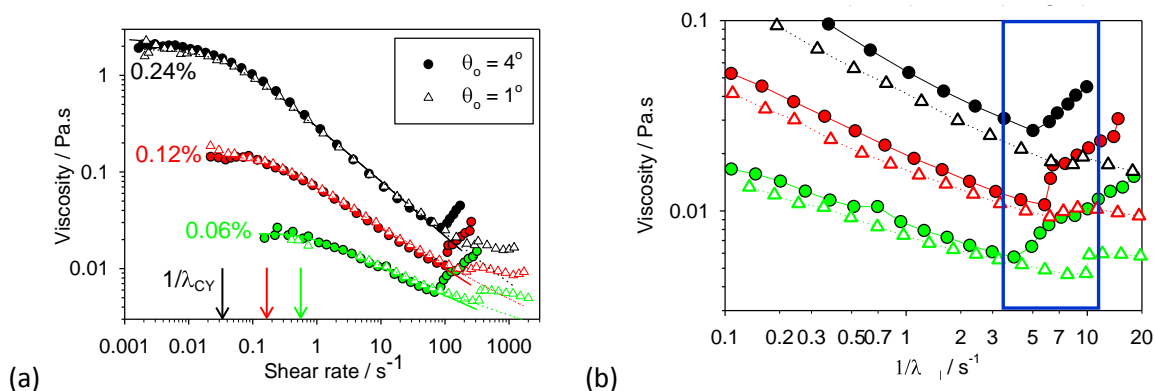

Figure 10 (a) Flow curves for 18MDa HPAM (3630S) at three concentrations measured using a cone-and-plate geometry at two cone angles. The onset of flow instability (onset in apparent thickening) is at significantly higher rate for the 1° cone angle but is independent of concentration. (b) When data are re-plotted as $1/\lambda$ (see text) onset rates lies within a factor of two for all concentrations and both cone angles

3.5 Combined data

In Figure 11 we replot the data of Figure 4a as a function of Weissenberg number where we have obtained the relaxation time, λ_{PM}, from the upturn in the cone-and plate data (Figure 4b) using equation (5) as described in section 3.4. Further, to illustrate the additional dissipation observed in porous flow compared to that in the rheometer, we plot the abscissa in the same way as for Figure 5; i.e. the ratio of the porous flow derived apparent viscosity and the Carreau-Yasuda fit to the stable-

flow part of the rheometer flow curves in Figure 4b as described in section 3.2. The resulting data collapse is highly suggestive that (i) the onset of flow fluctuations in both cases can be described by the same characteristic relaxation time and (ii) despite the significantly different deformation fields in the two cases, the same root instability is triggered.
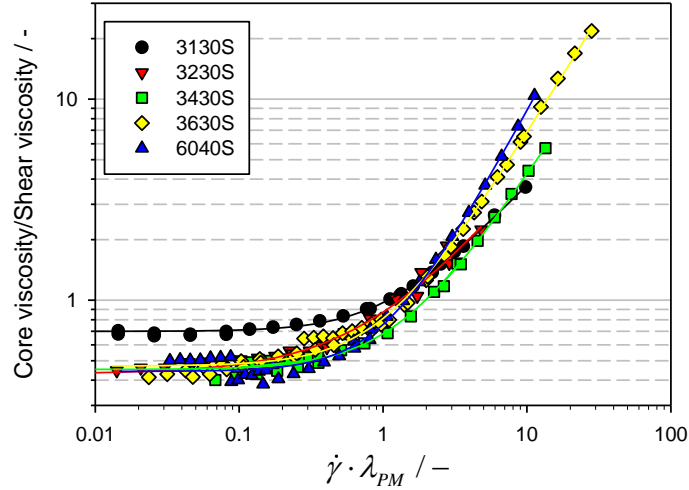

Figure 11 Porous flow data from Figure 4a divided by the Carreau-Yasuda fit to the low-shear and shear-thinning parts of the rheometric curves in Figure 4b, thereby highlighting the apparent flow thickening. The data are plotted against the Weissenberg number calculated using the characteristic time taken from the thickening observed in the cone-and plate-measurements. The data collapse suggests that the nature of the elastic turbulence onset observed in porous flow is closely related to the instability onset observed in the rheometer.

4   Discussion

When flowed through porous media, the studied HPAM solutions all exhibit an apparent thickening as flow rate (apparent shear rate) is increased (Figure 4). This increased dissipation rate is shown to be due to the onset of elastic turbulence [11] (Figure 6, Figure 7). For a given flow geometry, the onset of elastic turbulence is expected to scale with the Weissenberg number, Wi (see equation (6) and (7)) and hence to scale with a characteristic time associated with the polymer solution. In both flow through porous media (rocks and microfluidic devices) and in the cone-and-plate geometry we see a transition to elastic turbulence (for concentrations $c \geq 10c^*$) at a critical shear-rate (apparent or measured) corresponding to a characteristic time that scales as,

$$\lambda_{core}, \lambda_{PM} \propto \eta_S \cdot MW^2 \cdot c^0 ,\tag{12}$$

with λ_{core} and λ_{PM} the characteristic times in the rock core and cone-plate geometry, η_S the solvent viscosity, MW the polymer molecular weight and c the polymer concentration. For this set of polymer solutions, $N \propto MW$ and thus, comparing equation (11) and (12), we immediately see that the pertinent characteristic time, λ_{core}, is not a linear-viscoelastic relaxation time, $\lambda_{osc}, \lambda_{CY} \sim \tau_{rep} \sim MW^3 c^1$, and does not scale with the reptation time. Note though that all previous workers assume that the linear-viscoelastic relaxation time, λ_{osc} or λ_{CY}, is the time characterising the flow of these high molecular weight polymers in porous media. Importantly, we find instead an experimentally determined characteristic time for elastic turbulence onset that closely scales in the same way as either the Rouse time,

$$\tau_R \propto \eta_S \cdot N^2 \cdot c^0 ,\tag{13}$$

or equivalently as the dilute Zimm time (with $\nu \approx 2/3$),

$$\tau_Z \propto \eta_S \cdot N^{3\nu} \cdot c^0 ,\tag{14}$$

despite the solution being sufficiently concentrated to otherwise behave as a semi-dilute entangled system (i.e. scaling of $\eta(0)$, λ_{CY}, etc.).

Indications of the underlying cause for this apparent discrepancy can be seen in relaxation measurements of 2% (w/v) polyacrylamide solutions (5-6MDa) after a single extensional flow that have been reported experimentally [38] and theoretically [39]. The combination of experiment and theoretical analysis lead to a picture where the extensional flow stretches and aligns the polymer molecules such that the relaxation process from this configuration "is analogous to that considered in single-chain stretching experiments", i.e. the Rouse time. Although in these experiments elastic turbulence was neither looked for nor observed, they appear to support our observation that the transition to elastic turbulence is controlled by a characteristic time that scales as the Rouse (or Zimm) time. We might rationalise this behaviour by suggesting that the repeated periods of extension and shear that a fluid element experiences as it passes through a porous medium lead to a highly non-equilibrium, and possibly partially disentangled, configuration. Indeed Larson [40] points out "Although concentrated solutions and melts are usually strongly affected by entanglements, we see … that entanglement effects are weakened significantly at high strain rates, at which even concentrated solutions exhibit behaviours that resemble those of dilute solutions". Then, as in the references [38] [39], the initial relaxation from a non-equilibrium somewhat disentangled and aligned configuration is simply the Rouse time.

The Rolie-Poly constitutive model [17] was originally written to describe flow of polymer melts. The model views a full description of the flow properties as requiring two relaxation times: the first the reptation time that defines the (linear) relaxation time concerned with deformation of the entanglement configuration (i.e. without significantly perturbing the backbone random walk) and the second a Rouse time associated with relaxation of a straightened polymer backbone. These two characteristic times are required as a minimum to fully describe a melt flow. Hence a similar behaviour could also be expected for the entangled solutions in this study where, for strong flows, the behaviour would then be dominated by the Rouse time.

In a recent study, Reis and Wilson [41] explore theoretically instabilities arising for a Rolie-Poly liquid flowing through either an undulating channel or a slot-like constriction. In their work they identify two instabilities, one dominated by shear and the other by extension. The former is found to be well characterised by an M parameter derived using a Weissenberg number employing the reptation time, which is therefore interpreted as showing that streamline curvature is a dominant causal factor. For the instability observed in the extension-dominated flow they conclude that streamline curvature is not solely responsible and they interpret their data in terms of the smaller Weissenberg number defined with the Rouse time.

Within our porous media systems of rock core and microfluidic network we have both contraction-expansion flow and undulating channels. It is therefore difficult unambiguously to assign the observed behaviour to one or other of these instabilities. Nevertheless, it is clear that the model suggests an instability onset dependent on the Rouse timescale in addition to that determined by the reptation timescale. We do not see any evidence for a flow instability onset that scales with the reptation time, but we do see the onset of elastic turbulence that scales in the same way as the Rouse (freely draining chain) or Zimm (hydrodynamically interacting chain) times. Further, when comparing the flow of 3.5MDa HPAM solution (3130S) in two structures (see Appendix) we see that the onset of flow thickening, and therefore elastic turbulence, is deferred to higher deformation rates for the device where streamlines have less curvature. The ratio of onset deformation rates is approximately 4, whereas the ratio of Carreau-Yasuda relaxation time, λ_{CY}, ($\approx$ reptation time) and the fluctuation onset characteristic time, λ_{PM} ($\approx$Rouse time) is about 100. Hence the ratio of these measured onset rates (characteristic times) is much less than expected from the calculation.

The finding that concentration does not change the active relaxation timescale for the onset of elastic turbulence explains significant discrepancies in the literature where some workers attempted to vary "elasticity" by varying concentration [34] and others, including some field-scale experience in China [10], varied "elasticity" by varying molecular weight. In addition, equation (9) together with equation (12) allow, for a given rock permeability and imposed flow rate, the estimation

of a minimum polymer molecular weight required to cause a fluctuating flow field and hence enhanced displacement as shown in [11].

5   Conclusion

The onset of elastic turbulence for flow of high molecular weight partially hydrolysed polyacrylamides in porous media at practically used concentrations ($\geq 10c*$) is not determined by the linear viscoelastic relaxation time. Instead, a characteristic time that is independent of concentration and scales as MW^2, i.e. one that scales as does the Rouse time, is found to be appropriate over the range of concentrations studied. Whereas this behaviour is contrary to the expectation of many workers [31], [34], it may be rationalised as arising from a highly non-equilibrium flow-induced molecular configuration [38], [39]. Confirmation of this conjecture, for example through scattering experiments, would be of very great interest.

6   Acknowledgements

The authors would like to thank interns Miran Tsang and Katie Leeper from the University of Bristol for acquiring some of the datasets presented in this study together with J.R.Anthony Pearson for many detailed discussions.

7   Appendices

7.1   Linear viscoelasticity

The linear viscoelastic behaviour of the HPAM solutions are shown in Figure 12. Plotted in Figure 12(a) are the moduli for the concentration series of the 35 MDa HPAM 6040S corresponding to the samples in Figure 3. As expected, the curves shift to higher modulus and lower frequency with increasing concentration. The data for solutions with $\eta(0) \approx 2$ Pa.s described in Figure 4 are shown as frequency sweeps in Figure 12(b). As the MW increases (and correspondingly the concentration falls as $\sim MW^{-1}$) the $G'=G''$ relaxation time λ_{osc} increases (crossover frequency falls) and value of the moduli decreases with exponents close to 2 (bottom).
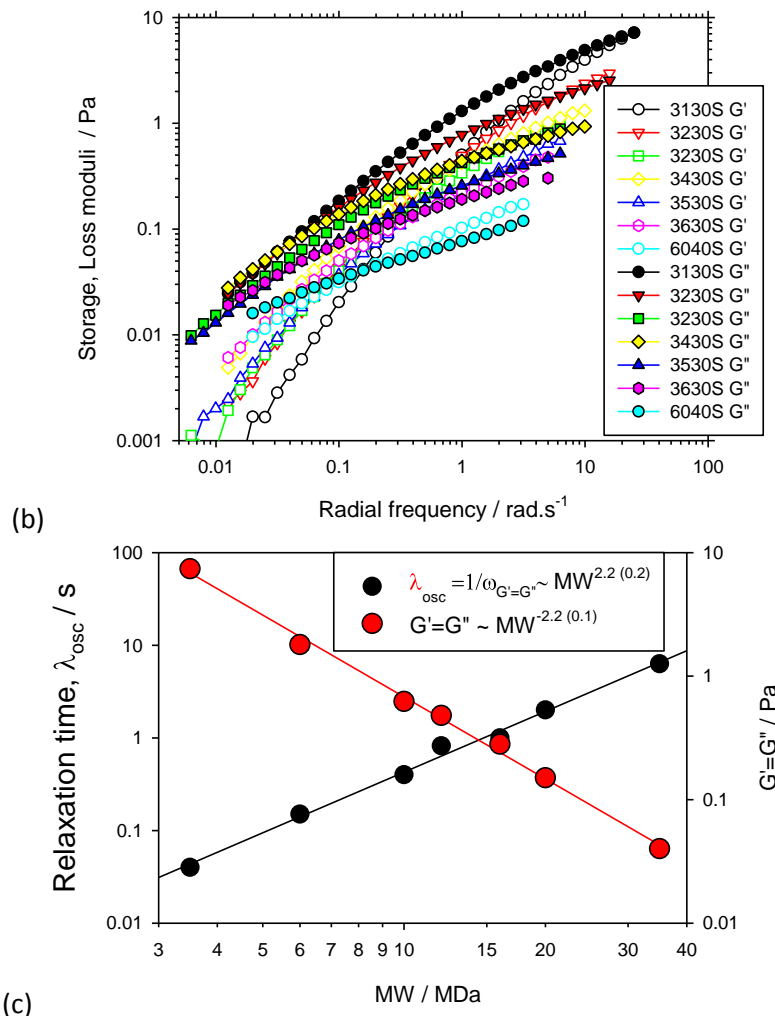

(a)

(b)

(c)
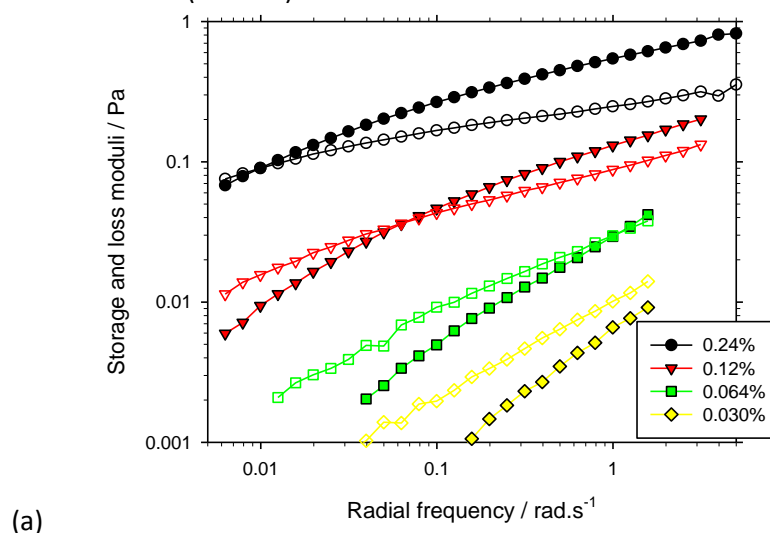
Figure 12 Oscillatory frequency sweep studies of HPAM solutions. (a) 35 MDa sample at concentrations $0.03 - 0.24\%$ w/w. Filled symbols G', open symbols G''. (b) HPAM solutions of MW 3.6 (3130S) to 35 MDa (6040S) at concentrations corresponding to $\eta(0) \approx 2$Pa.s. Filled symbols G'', open symbols G'. (c) Relaxation time $(1/\omega)$ and modulus values at $G'=G''$ for 2 Pa.s solutions.

7.2   Micromodel design

We examined the onset of flow thickening in two microfluidic devices, Figure 13. In the first device (MM2) the average channel width connecting pores is 75µm. MM2 has channels oriented at 45° to the average flow direction within the device and the pores (200µm square) are larger than the channels. Thus in MM2 in order to estimate the Weissenberg number, we calculate the shear rate as the average local velocity divided by the channel half-width, and to estimate the Deborah number we divide the local velocity by half the pore to pore distance. For MM2 we obtain M = Wi(37.5/176) using equation (7).   For the second device (MM1) the channel size is a little larger (100µm).   The characteristic flow length is however not so obvious since the channels are oriented along the flow direction. However, if we assume that the onset of apparent flow thickening starts at the same value of M, then using equation (7),

$$\frac{Wi_{MM1}}{Wi_{MM2}} = \left(\frac{a_{MM2}}{a_{MM1}} \cdot \frac{L_{MM1}}{L_{MM2}} \right)^{1/2}, \qquad (15)$$

where subscripts indicate the device for that parameter and the Weissenberg numbers are calculated at the apparent flow thickening onset. Using equation (15), we find $L_{MM1} \approx 8000$µm. With streakline photography we see particles traverse several periods of the lattice before turning from the straight through direction, suggesting this value to be reasonable.
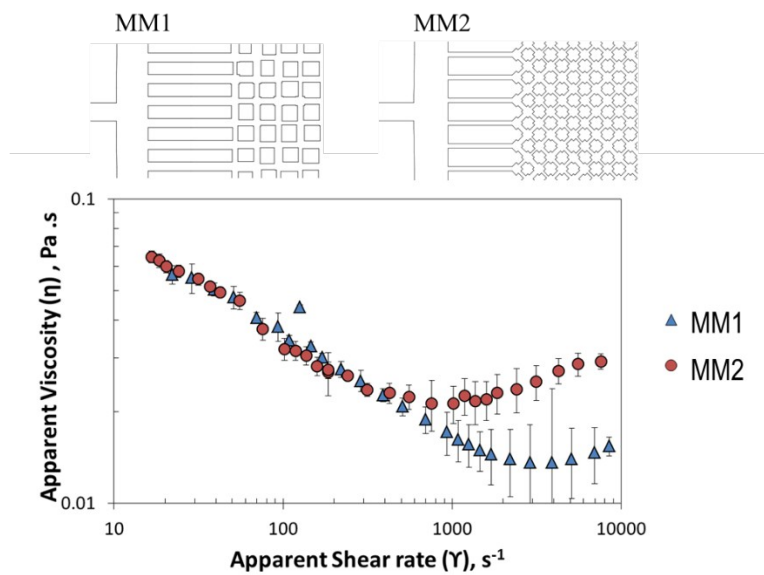
Figure 13 Apparent viscosity measured for a 0.6wt% solution of 3.6MDa HPAM (3130S) in each of two different microfluidic devices, MM1 and MM2. The onset of flow thickening is brought to lower apparent shear rates for the MM2 structure for which streamlines have tighter curvature.

8 References

[1]   J. Bear, Dynamics of Fluids in Porous Media, New York: Dover, 1988.

[2]   A. F. Morais, H. Seybold, H. J. Hermann and J. S. Andrade, "Non-Newtonian Fluid Flow through Three-Dimensional Disordered Porous Media," *PRL,* vol. 103, no. 19, p. 194502, 2009.

[3]   K. T. Tallakstad, H. A. Knudsen, T. Ramstad, G. Lovoll, K. J. Maloy, R. Toussaint and E. G. Flkkoy, "Steady-State Two-Phase Flow in Porous Media: Statistics and Transport Properties," *PRL,* vol. 102, no. 7, p. 074502, 2009.

[4]   M. Brust, C. Schaefer, R. Doerr, L. Pan, M. Garcia, P. E. Arratia and C. Wagner, "Rheology of human blood plasma: Viscoelastic versus Newtonian behavior," *PRL,* vol. 110, no. 7, p. 078305, 2013.

[5]   F. Gritti, A. Cavazzini, N. Marchetti and G. Guiochon, "Comparison between the efficiencies of columns packed with fully and partially porous C18-bonded silica materials," *Journal of Chromatography A ,* vol. 1157, no. 1-2, pp. 289-303, 2007.

[6]   K. S. Lackner, "A guide to CO2 sequestration," *Science,* vol. 300, no. 5626, pp. 1677-1678, 2003.

[7]   L. W. Lake, Enhanced Oil Recovery, Prentice-Hall, 1989.

[8]   D. Wang, J. Cheng, W. Gong, Q. Yang, Q. Li and F. Chen, "Viscous-Elastic Polymer Can Increase Microscale Displacement Efficiency in Cores," *SPE Journal,* p. SPE 63227, 2000.

[9]   D. Wang, H. Xia, S. Yang and G. Wang, "The Influence of Visco-elasticity on Micro Forces and Displacement Efficiency in Pores,Cores and in the field," *SPE Journal,* p. 127453, 2010.

[10]   H. Z. Dong, S. F. Fang, D. M. Wang, J. Y. Wang, Z. Liu and W. H. Hong, "Review of Practical Experience & Management by Polymer Flooding at Daqing," *SPE Journal,* p. SPE 114342, 2008.

[11]   A. Clarke, A. M. Howe, J. Mitchell, J. Staniland, L. Hawkes and K. Leeper, "Mechanism of anomalously increased oil displacement with aqueous viscoelastic polymer solutions," *Soft Matter,* 2015.

[12]   V. Steinberg and A. Groisman, "Elastic versus inertial instability in Couette-Taylor flow of a polymer solution: Review," *Philosophical magazine. B ,* vol. 78, no. 2, pp. 253-263, 1998.

[13]   A. N. Morozov and W. van Saarloos, "An introductory essay on subcritical instabilities and the transition to turbulence in visco-elastic parallel shear flows," *Physics Reports,* vol. 447, pp. 112-143, 2007.

[14]   A. Groisman and V. Steinberg, "Elastic turbulence in a polymer solution," *Nature,* vol. 405, p. 53, 2000.

[15]   A. Groisman and V. Steinberg, "Elastic turbulence in curvilinear flows of polymer solutions," *New Journal of Physics,* vol. 6, p. 29, 2004.

[16]   D. F. James, "Boger Fluids," *Annu. Rev. Fluid Mech,* vol. 41, pp. 129-142, 2009.

[17]   A. E. Likhtman and R. S. Graham, "Simple constitutive equation for linear polymer melts derived from molecular theory: Rolie–Poly equation," *J. Non-Newtonian Fluid Mech. ,* vol. 114, pp. 1-12, 2003.

[18]   R. S. Graham, A. E. Likhtman, T. C. McLeish and S. T. Milner, "Microscopic theory of linear, entangled polymer chains under rapid deformation including chain stretch and convective constraint release," *J. Rheol.,* vol. 47, no. 5, pp. 1171-1200, 2003.

[19]   A. V. Dobrynin, R. H. Colby and M. Rubinstein, "Scaling Theory of Polyelectrolyte Solutions," *Macromolecules,* vol. 28, pp. 1859-1871, 1995.

[20]   R. Lindken, M. Rossi, S. Grosse and J. Westerweel, "Micro-Particle Image Velocimetry (mPIV): Recent developments,applications and guidelines," *Lab on a Chip,* vol. 9, pp. 2551-2567, 2009.

[21]   H. Darcy, Les Fontaines Publiques de la ville de Dijon, Dalmont, Paris, 1856.

[22]   C. L. Perrin, P. M. Tardy, K. S. Sorbie and J. C. Crawshaw, "Experimental and modeling study of Newtonian and non-Newtonian fluid flow in pore network micromodels," *J. Coll. Interf. Sci.,* vol. 295, pp. 542-550, 2006.

[23]   T. Sochi, "Flow of Non-Newtonian Fluids in Porous Media," *Journal of Polymer Science: Part B: Polymer Physics,* vol. 48, pp. 2437-2767, 2010.

[24]   X. Lopez, P. H. Valvatne and M. J. Blunt, "Predictive network modeling of single-phase non-Newtonian flow in porous media," *J. Coll. Interf. Sci.,* vol. 264, pp. 256-265, 2003.

[25]   X.-B. Li, F.-C. Li, W.-H. Cai, H.-N. Zhang and J.-C. Yang, "Very-low-Re chaotic motions of viscoelastic fluid and its unique applications in microfluidic devices: A review," *Experimental Thermal and Fluid Science,* vol. 39, pp. 1-16, 2012.

[26]   J. Zilz, R. J. Poole, M. A. Alves, D. Bartolo, B. Levache and A. Linder, "Geometric scaling of a purely elastic flow instability in serpentine channels," *Journal of Fluid Mechanics,* vol. 712, pp. 203-218, 2012.

[27]   G. H. McKinley, P. Pakdel and A. Oztekin, "Rheological and geometric scaling of purely elastic flow instabilities," *J. Non-Newtonian Fluid MEch.,* vol. 67, pp. 19-47, 1996.

[28]   P. Pakdel and G. H. McKinley, "Elastic instability and curved streamlines," *PRL,* vol. 77, no. 12, p. 2459, 1996.

[29]   D. O. Olagunju, "Elastic instabilities in cone-and-plate flow: Small gap theory," *Z angew Math Phys,* vol. 46, pp. 946-959, 1995.

[30]   D. J. Holland, J. Mitchell, A. Blake and L. F. Gladden, "Grain Sizing in Porous Media using Bayesian Magnetic Res onance," *PRL,* vol. 110, p. 018001, 2013.

[31]   D. Delshad, D. H. Kim, O. A. Magbagbeola, C. Huh, G. A. Pope and F. Tarahhom, "Mechanistic interpretation of viscoelastic behavior of polymer solutions for improved polymer-flood efficiency," *SPE journal,* p. 113620, 2008.

[32]   R. S. Seright, T. Fan, K. Wavrik and R. d. C. Balaban, "New insights into polymer rheology in porous media," *SPE Journal,* p. 129200, 2011.

[33]   T. Burghelea, E. Segre, I. Bar-Joseph, A. Groisman and V. Steinberg, "Chaotic flow and efficient mixing in a microchannel with a polymer solution," *Phys. Rev. E,* vol. 69, p. 066305, 2004.

[34]   E. C. Vermolen, M. J. T. Haasterecht and S. K. Masalmeh, "A systematic study of the polymer visco-elastic effect on residual oil saturation by core flooding," *SPE Journal,* no. SPE-169681, 2014.

[35]   A. Groisman and S. R. Quake, "A Microfluidic Rectifier: Anisotropic Flow Resistance at Low Reynolds Numbers," *PRL,* vol. 92, no. 9, p. 094501, 2004.

[36]   R. H. Colby, "Structure and linear viscoelasticity of flexible polymer solutions: Comparison of polyelectrolyte and neutral polymer solutions," *Rheo. Acta,* vol. 49, no. 5, pp. 425-442, 2010.

[37]   K. Grass and C. Holm, "Polyelectrolytes in electric fields: measuring the dynamical effective charge and effective friction," *Soft Matter,* vol. 5, pp. 2079-2092, 2009.

[38]   U. A. Klessinger, B. K. Wunderlich and A. R. Bausch, "Transient flow behavior of complex fluids in microfluidic channels," *Microfluid Nanofluid,* vol. 15, pp. 533-540, 2013.

[39]   S. Litvinov, X. Hu, M. Ellero and N. Adams, "Mesoscopic simulation of the transient behavior of semi-diluted polymer solution in a microchannel following extensional flow," *Microfluid Nanofluid,* vol. 16, pp. 257-264, 2014.

[40]   R. G. Larson and P. S. Desai, "Modeling the Rheology of Polymer Melts and Solutions," *Annu Rev. Fluid Mech.,* vol. 47, pp. 47-65, 2015.

[41]   T. Reis and H. J. Wilson, "Rolie-Poly fluid flowing through constrictions: Two distinct instabilities," *J. Non-Newt. Fluid Mech.,* vol. 195, pp. 77-87, 2013.

[42]   M. Rubinstein and R. H. Colby, Polymer Physics, Oxford University Press, 2003.